

# **Novel Multi-Band Plasmon Filters based on Double-Band Surface Plasmon Polarizations**

**Abdollah Abertavi, Masoud Jabbari\* and Ghahraman Solookinejad**

*Department of Electrical Engineering, Marvdasht Branch,  
Islamic Azad University, Marvdasht, Iran*

\*Corresponding author: masoudjabbari@yahoo.com

Received 10/04/2024; accepted 21/09/2024

<https://doi.org/10.4152/pea.2026440303>

---

## **Abstract**

The background motivation of this paper was SPP, which refers to surface waves occurring at terahertz frequencies, as widely used wave in optics industry. This wave has been produced during the electromagnetic field interaction with oscillations of free metal electrons. Due to their improved field and intense incarceration close to the metal surface, SPP waves have been extensively employed for high sensitivity sensors and small photonic circuits. The method herein proposed was a BPF based on designer-SPP by means of central frequency and adjustable bandwidth. It was adjusted via varactor diodes placed in different positions in the T-shaped resonator. Considering the constraints and strengths of high field SPP polarizations, hearing and coupling becomes weaker than that from the usual microstrip. Analytical and evaluation methods comprised three inductors assessed at different locations of the T-shaped resonator, which were controlled by DC bias voltage. Transition from the microstrip QTEM mode to SPP misleading mode was performed to excite SSPP based on the T-shaped resonator with g-distance coupling.

**Keywords:** adjustable central frequency; BPF; QTEM, SPPP.

---

## **Introduction\***

SPP emits an electromagnetic wave at dielectric-conductor interface caused by the light coupling to collective electron oscillation [1]. As for its special feature, SPP allows the diffraction constraint and light manipulation within sub-wavelength scales to break, then strengthening field concentration. Hence, SPP has been widely used in a wide variety of optical communications, photonic and sensing fields [2-5]. SPP specific features such as slow-wave behavior and field limitations other than optical frequency regime allow for significant progress of components and devices. Due to SPP natural occurrence in optical frequencies, different concepts can be defined for this phenomenon in microwaves and terahertz frequency ranges. SSPP

---

\*The abbreviations list is in page 198.

mediates electromagnetic waves surface disseminating through ridged metallic surfaces at microwave frequency [6, 7].

BPF is the initial/final component of RF/microwave systems. Recent advances in demand for modern wireless communication and radar applications are high-performance and dynamic control RF subsystems. Therefore, adjustable microwave filters are interesting for researchers and electronic engineers. Conventional microwave filters typically employ traditional micro-strip technology which affects radiation and hearing loss and interconnection problems. Alignment between transmission lines is involved in results and signal accuracy, which can reduce RF systems quality [8]. SSPP based on RF systems are an alternative solution to overcome this issue [9, 10]. SPP is a surface electromagnetic wave closely related to the consistent oscillations of free-electron density at the dielectric-metal interface, being found at near-infrared and optical frequencies. They exponentially decay in the direction perpendicular to the interface in which the constraint and increase of the field below the wavelength appears [11, 12].

Since metals behave like plasma, with a negative transmittance at light frequency, SPP wave is supported by a metal-dielectric interface. However, metals are full conductors at microwave and terahertz frequencies. Therefore, exotic properties are not usually found in this frequency range. Recently, it has been revealed that semi-metals such as graphene and semiconductors naturally support SPP at terahertz frequency, which can be used in optoelectronic devices such as solar cells, graphene sensors and other nanophotonic and plasmonic devices [13-15].

However, to understand SPP-like properties in the closeness of the metal-dielectric interface at microwave and terahertz frequencies, plasmonic metamaterials [16] proposed as ultra-long wavy metal surfaces with 2-dimensional cavities or 1-dimensional grooves are called SPP makers. The scattering curve and cutoff frequency for such a structure can be modified by physical parameters. Thus, these structures can conduct and manipulate electromagnetic waves at the sub-wave scale, which can be used to design transmission lines [17, 18] and filters [19-21], withal to excite antennas [22], amplifiers [23], terahertz switches [24] and adjustable filters [25-29].

In [25, 28], an adjustable band-stop behavior has been analyzed via changing the physical dimensions. In [26], a new SSP-TL was proposed based on the capacitor loading technique that makes it more flexible and adaptable to dispersion control, which requires thinner line-width than from the conventional type to achieve a very slow and quietly applicable wave for compact systems. Even so, the presented structure in [25-27, 30] requires manual time adjustment with different parameter values to adjustable features. In [29], an adjustable BPF has been proposed based on transmission lines to control low-high cut-off frequencies of the filter which is too large and complex for the operational prototype.

In this regard, this paper aimed to design a new two-layer and one-sided wavy-based BPF structure to transfer multiple bands. The cut-off frequency of all bands depends on different modes of approximate frequency of SSPP which were easily adjusted by the grooves depth. The proposed structure was adjusted using varactor diodes placed in different positions in the T-shaped resonator. Considering constraints and strengths of high field SPP polarizations, hearing and coupling was weaker than that from the usual microstrip. Three inductors were considered at different locations of the T-shaped resonator, which were controlled by DC bias voltage. Transition from the microstrip QTEM mode to the misleading mode of SPP was performed to excite SSPP based on the T-shaped resonator with g-distance coupling.

Main contributions were briefly described by as follows: BPF based on designer-SPP using central frequency and adjustable bandwidth; varactor diodes with different positions in the T-shaped resonator; three inductors with different locations of the T-shaped resonator; transition from the microstrip QTEM to SPP misleading mode.

### Surface polariton plasmon and its stimulation strategy

Plasmon, in the classical definition, is the mass oscillation of free electrons which is described with respect to constant positive ions in a metal. SPP are surface electromagnetic waves, including surface charges, that propagate along the metal-dielectric interface. How to excite surface loads? A polarized wave (p) reaches a flat interference plane at the collision angle ( $\theta_1$ ). The shock wave has a photon momentum ( $\hbar k_d$ ) in the dielectric with a refractive index ( $n_d$ ). When the wave reaches the interference surface, it is propagated by reflecting waves at angles equal to the incident angle, and the momentum of the photons remains constant. In addition, the wave propagates through the metal in a new direction with a refractive angle ( $\theta_2$ ). Photon momentum is  $\hbar k_m$ , whereas  $k_m = 2\pi n_m/\lambda$  and  $n_m$  is the refractive metal index. Momentum components are constant along  $x$  direction. So,  $k_{dx} = k_{mx}$ , that  $k_{dx} = k_d \sin \theta_1$  and  $k_{mx} = k_m \sin \theta_2$ . Snell's law can be presented as follows:

$$n_d \sin \theta_1 = n_m \sin \theta_2 \quad (1)$$

In general, the dielectric refractive index ( $n_d$ ) is larger than the metal type ( $n_m$ ) in visible spectrum [31]. Since  $n_d > n_m$ , the maximum value of  $\theta_2$  is  $90^\circ$ , and  $\theta_1$  is restricted. Beyond the angle limit, the wave cannot propagate through the metal, in which case the limited impact angle is called critical angle ( $\theta_c$ ) where:  $\sin \theta_c = n_m/n_d$ . The momentum of a wave along the surface with an angle of impact higher than  $\theta_c$  is greater than what can be supported by a. For p-polarized impact waves on the metal surface, the oscillating electric field creates surface charges at the metal-dielectric interface, and the surface charges will be under a collective oscillation. Although the wave is completely reflected on the interface, due to oscillating loads, radiation fields penetrate into the metal. Evanescent fields are perpendicular to the interface (Fig. 1).

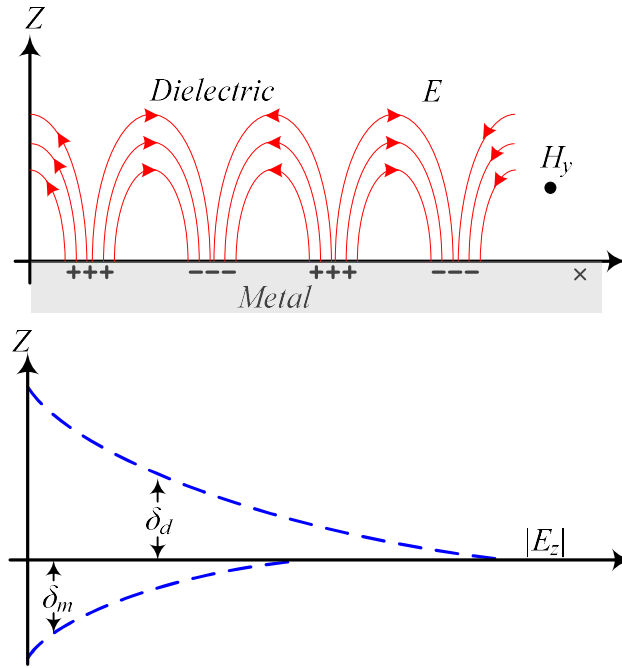


**Figure 1:** Schematics of SPP propagation between metal and air.

At the critical angle, the decremented length goes to infinity, but as the angle further increases, it rapidly decreases to the light wavelength. In these cases, the evanescent fields are more suitable for the incidence wave than the critical angle for the radiation coupling with the SPP.

Since there is no vertical boundary on  $E_x$ , this component is fixed along the boundary. However, in the case of  $E_z$  there is no component perpendicular to  $E$ ,  $D_z$  is a continuous component of  $D$  (there is no free charge) and  $E_z$  has to change if  $\epsilon$  changes because:  $D_z = \epsilon_d \epsilon_0$  and  $E_{zd} = \epsilon_m \epsilon_0 E_{zm}$ . This discontinuity in  $E_z$  leads to polarized loads at the interference surface. From these simple assumptions, it is clear that polarized impact radiation does not normally cause load on an interfering surface. P-polarized wave automatically generates time-dependent polarized loads on the interfering surface. Being vertical E fields are needed to create surface charges; it is essential to consider P-polarized electromagnetic waves. In addition, the surface wave in any form must satisfy the electromagnetic wave equation in the two materials. If the plane x-y is an interference plane, for the wave propagated in the x direction as  $z > 0$ :

$$\begin{aligned} E_d &= (E_{xd} \cdot 0 \cdot E_{zd}) \exp(-k_{zd}z) \exp[i(k_x x - \omega t)] \\ H_d &= (0 \cdot H_{yd} \cdot 0) \exp(-k_{zd}z) \exp[i(k_x x - \omega t)] \end{aligned} \quad (2)$$

when  $z < 0$  and also:

$$\begin{aligned} E_m &= (E_{xm} \cdot 0 \cdot E_{zm}) \exp(-k_{zm}z) \exp[i(k_x x - \omega t)] \\ H_m &= (0 \cdot H_{ym} \cdot 0) \exp(-k_{zm}z) \exp[i(k_x x - \omega t)] \end{aligned} \quad (3)$$

Using Eqs. (2) and (3) in Maxwell's equation,  $\nabla \cdot \mathbf{E} = 0$ , electric field can be presented components as follows:

$$\begin{aligned} E_{zd} &= i \frac{k_x}{k_{zd}} E_{xd} \\ E_{zm} &= -i \frac{k_x}{k_{zm}} E_{xm} \end{aligned} \quad (4)$$

Considering Eq. (2) and Maxwell equation in the form  $\nabla \times \mathbf{E} = -c^{-1} \partial \mathbf{H} / \partial t$ :

$$\begin{aligned} -k_{zd} E_{xd} - i k_x E_{zd} &= i k H_{yd} \\ k_{zm} E_{xm} - i k_x E_{zm} &= i k H_{ym} \end{aligned} \quad (5)$$

Then, finally, Eq. 6 can be attained:

$$\begin{aligned} \varepsilon_d k E_{xd} &= i k_{zd} H_{yd} \\ \varepsilon_m k E_{xm} &= -i k_{zm} H_{ym} \end{aligned} \quad (6)$$

where:

$$\begin{aligned} k_{zd}^2 &= k_x^2 - \varepsilon_d k^2 \\ k_{zm}^2 &= k_x^2 - \varepsilon_m k^2 \end{aligned} \quad (7)$$

In addition, it must be noted that tangent components (E and H) are continuous, according to boundary conditions of electromagnetic fields at  $z = 0$ , i.e.,  $E_{xd} = E_{xm}$  and  $H_{yd} = H_{ym}$ . The relationship between dielectric constants and normal components of the wave vector will be:  $k_{zd} / k_{zm} = -\varepsilon_d / \varepsilon_m$ . Then:

$$k_x = k \sqrt{\frac{\varepsilon_d \varepsilon_m}{\varepsilon_d + \varepsilon_m}} \quad (8)$$

Considering  $k_{xpp}$  instead of  $k_{xpp}$ , SPP scattering equation can be presented as follows:

$$k_{SPP} = k \sqrt{\frac{\varepsilon_d \varepsilon_m}{\varepsilon_d + \varepsilon_m}} \quad (9)$$

SPP scattering curve shows nonlinear properties, which are portrayed in Fig. 2.

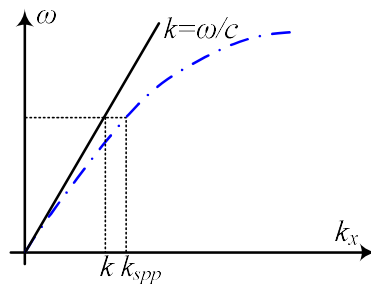


**Figure 2:** scattering curves of a SPP wave.

$\hbar k_{spp}$  momentum of SPP wave is greater than the one from light in open space photons ( $\hbar k$ ), for the same frequency ( $\omega$ ), which causes a mismatch between them. This mismatch must be overcome by coupling SPP and light modes at the interface, when  $\epsilon_d + \epsilon_m = 0$ .

Surface loads generate mass oscillations to excite SPP. Dielectric constant of metal ( $\epsilon_m$ ) has the shape of a free electron:

$$\epsilon_m = 1 - \frac{\omega_p^2}{\omega^2} \tag{10}$$

where  $\omega_p$  is bulk plasma frequency. For many metals, the frequency is in ultraviolet wavelength range, whereas the metal is not above that frequency. According to Eq. (10), SPP frequency can be attained by:

$$\omega_{spp} = \frac{\omega_p}{\sqrt{1 + \epsilon_d}} \tag{11}$$

It can be seen that SPP frequency is lower than that from bulk plasma. Above-described SPP excitation occurred at the dielectric-metal interface. In contrast, a thick metal film bounded by a dielectric can excite two independent SPP waves at the dielectric-metal interface. In this case, the evanescent fields of the two non-coupled SPP waves inside the metal cannot overlap [3]. In case of a thin enough metal film, the evanescent fields of the two SPP waves inside the metal can overlap. Then, two SPP waves coupled at the interface appear. As a result, SPP waves are converted into super coupled modes, symmetric (low frequency) and asymmetric mode (high frequency), with a transverse electric field distribution. Fig. 3 shows the metal bound between the dielectric and the interface, and SPP excitation state, in both cases .

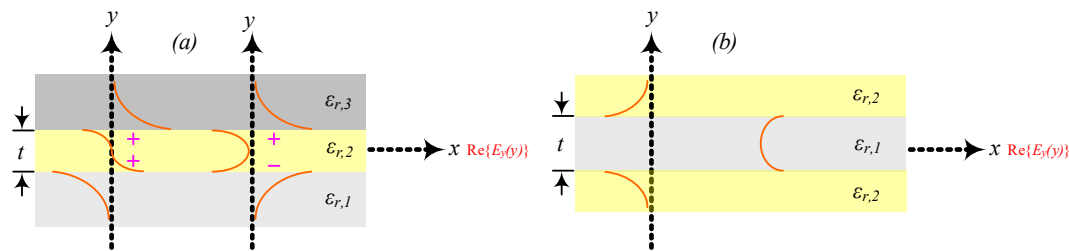


**Figure 3:** (a) Metal sheet ( $\epsilon_{r,2}$ ) and thickness ( $t$ ) bounded by semi-infinite dielectrics ( $\epsilon_{r,1}$ ,  $\epsilon_{r,3}$ ) and SPP two modes of ( $a_b$ ,  $s_b$ ); (b) Dielectric sheet ( $\epsilon_{r,1}$ ) with  $t$  bounded by semiconductor metals ( $\epsilon_{r,2}$ ) and a symmetric bound mode.

Thus, the electric field drop is very small in symmetric SPP mode, because it penetrates deeply into the dielectric. Thus, electric fields attenuation is much less than that of SPP at the single interface. Thus, symmetric SPP mode is also called

LRSP, i.e., its propagation length is 138 times longer than that from individual SPP [32]. However, the electric field drop is significant in asymmetric SPP mode, since electric fields are primarily concentrated within the metal, and SPP modes show increasing limitations. Thus, asymmetric SPP mode is basically called SRSPP, and the propagation length is very short, due to the very strong damping (strong ohmic drops) in the metal [33].

### Theory and principle of multi-band plasmon filter

In this work, a BPF based on designer-surface plasmon polarizations was structured using central frequency and bandwidth adjusted using varactor diodes and placed in different positions in the T-shaped resonator. The theory and principles of the proposed filter were inhere explained.

#### Design theory and principles

Fig. 4 shows SPP's T-shaped resonator along with equivalent circuits to odd and even modes. This T-shaped resonator was provided as two  $\lambda_g/4$  resonators coupled via  $K$  inverter provided by SSPP's transmission line section. Electrical length (degree) and conductance ( $1/\Omega$ ) were in one part of the line ( $\varphi_1/2, Y_1$ ) and on another one ( $\varphi_k, Y_l$ ). Each wavy transmission line with metal strips on it has an electrical length ( $\Delta\varphi'$ ) and conductance ( $\Delta Y'$ ). By adjusting the taps' length, which can be longer or shorter than  $\lambda_g/4$ , a zero transmission can be generated at a frequency lower or higher than the desired pass band. Since the groove length is less than  $\lambda_g/4$ , thus, a zero transmission is produced in the higher stop band.

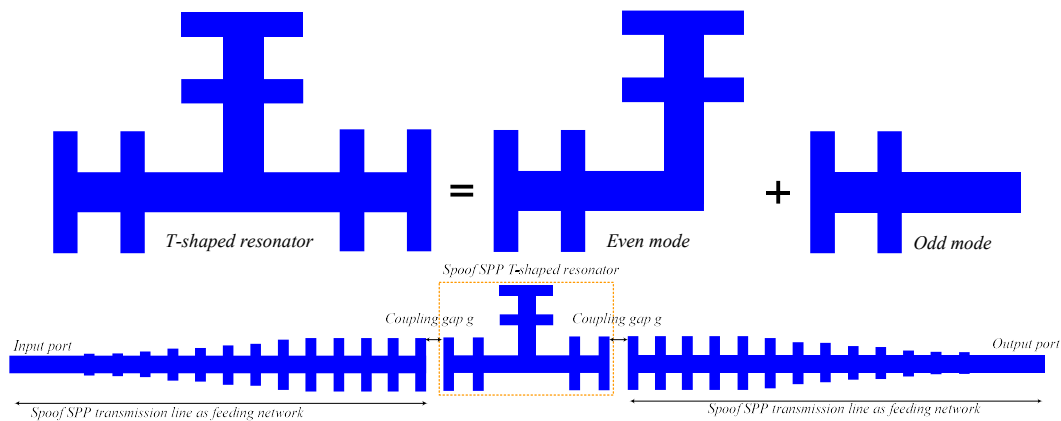


**Figure 4:** T-shaped resonator of SPP along with the equivalent circuits to odd and even modes.

In the designed resonator, resonance condition is defined as follows:

$$Img[Y_{ine}] = 0 \tag{12}$$

where  $Y_{ine}$  is the conductance of even mode which is defined by:

$$\begin{aligned}
 Y_{ine} &= Y_1 \left[ \frac{Y_M + jY_1 \tan(\phi_1/2)}{Y_1 + jY_M \tan(\phi_1/2)} \right] + n^*(jY' \tan \Delta\phi') \\
 Y_M &= j \frac{Y_1}{2} \tan \phi_k + m^*(j\Delta Y' \tan \Delta\phi') \\
 \text{Im}g[Y_{ino}] &= 0
 \end{aligned}
 \tag{13}$$

where  $n = 4$  and  $m = 2$ .  $Y_{ino}$  are the conductance of an individual mode defined by:

$$Y_{ino} = -j Y_1 \cot\left(\frac{\phi_1}{2}\right) + n^*(\Delta Y' \tan \Delta\phi')
 \tag{14}$$

As for Eqs. (12) and (13), it is clear that  $\phi_1$  affects both even and odd modes, while  $\phi_k$  only influences even mode. Therefore, by adjusting physical length, equivalent electrical path for different frequency and even state frequencies can be changed.

**Power supply network design**

SSPP T-shaped resonator is directly coupled to the power supply transition line of SPP at the input and output (Fig. 4). This transmission line must contain cellular arrays. SSPP behavior was analyzed by scatter plots. Emission characteristics of SSPP guided modes were controlled by its structural parameters, i.e., distance between two grooves ( $d$ ), groove height ( $h$ ), metal thickness ( $t$ ) and lattice constant ( $p$ ). Dispersion properties of SSPP unit cell were obtained by numerical simulation, using CST MWS.

**Design of SSPP T-shaped resonator with odd-even mode analysis**

Fig. 5 shows a schematic of proposed adjustable T-resonator with an odd-even mode equivalent circuit. Two varactor diodes (C) and one (C1) were symmetrically placed in X and Y directions and on XY plane in the resonator.

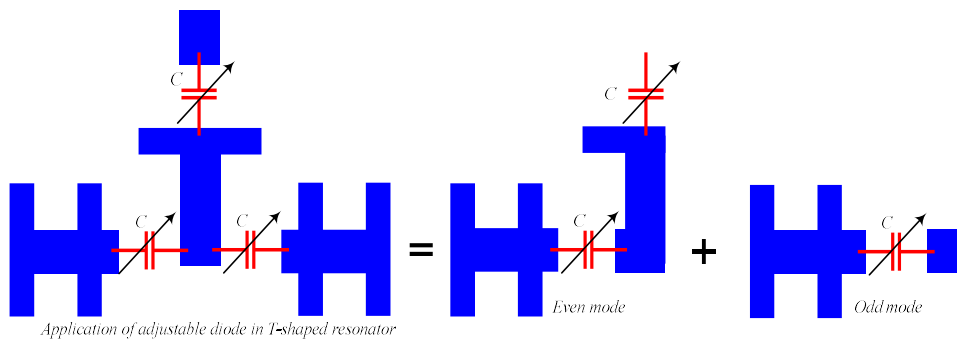


**Figure 5:** Schematic of the proposed adjustable T-resonator with an odd-even mode equivalent circuit.

Resonance schemes for the proposed resonator were obtained by:

$$\begin{aligned}
 \text{Im}g[Y_{ine}] &= 0 \\
 \text{Im}g[Y_{ino}] &= 0
 \end{aligned}
 \tag{15}$$

where  $Y_{ine}$  and  $Y_{ino}$  are conductance of even and odd modes, respectively, being defined as follows:

$$Y_{in} = Y_1 \left[ \frac{Y'_M + jY_1 \tan(\phi_A)}{Y_1 + jY'_M \tan(\phi_A)} \right] + n^*(j\Delta Y' \tan \Delta\phi') \quad (16)$$

where  $Y_{ine} = Y_{in}$ , in case of:

$$Y'_M = \frac{Y_M * j\omega C}{Y_M + j\omega C}$$

$$Y_M = \frac{Y_1}{2} \left[ \frac{j\omega C_1/2 + j \frac{Y_1}{2} \tan(\phi_k)}{\frac{Y_1}{2} + j(j\omega C_1/2 \tan(\phi_k))} \right] + (j\Delta Y' \tan \Delta\phi') \quad (17)$$

where  $Y_{ino} = Y_{in}$  while  $Y'_M = j\omega C$ .

For odd and even mode admissions, conductance matrix was expressed as:

$$Y = \begin{bmatrix} Y_{11} & Y_{12} \\ Y_{21} & Y_{22} \end{bmatrix} = \begin{bmatrix} \frac{(Y_{ine} - Y_{ino})}{2} & \frac{(Y_{ine} + Y_{ino})}{2} \\ \frac{(Y_{ine} + Y_{ino})}{2} & \frac{(Y_{ine} - Y_{ino})}{2} \end{bmatrix} \quad (18)$$

In addition, transmission zeros were expressed in conductance parameter terms as:

$$Y_{12} = Y_{21} = (Y_{ine} + Y_{ino})/2 = 0 \quad (19)$$

According to Eq. (15), varactor  $C$  affected both odd and even modes, whereas varactor  $C_l$  only affected even mode. Since varactor  $C$  simultaneously affected both modes, central frequency of the degenerative mode was generally varied by changing bias voltage around it. That way,  $V_{Cl}$  was essentially considered constant and bias voltage ( $V_C$ ) around varactor  $C$  changed, in which case the central frequency shifted. Then,  $V_C$  was considered constant and bias voltage of diodes  $C_l$  changed. Since  $C_l$  only affected even mode wave, degenerative mode split and bandwidth was adjusted. Also, modulation analysis was performed to design BPF. Signal distortion based on two-tone method was proposed for it [34]. Simulated modulation product was obtained by using ADS harmonic equilibrium simulation around the lowest frequency ( $f_0$ ) of the adjustable region. The two cases were distinguished by  $\Delta f$ , being located at frequencies  $f_1 = f_0 - \Delta f/2$  and  $f_2 = f_0 + \Delta f/2$ .

## Discussion of simulation results

### Power supply network design results

The T-shaped resonator was directly connected to the SSPP transmission line at the input and output, as shown in Fig. 4. This transmission line contains alternating arrays of unit cell (Fig. 6). SSPP behavior was portrayed by the scattering diagram, where the blue line indicates emission wave vector ( $k_0$ ) for the freely propagated wave and the green curve indicates emission wave vector ( $k_y$ ) for SSPP unit cell.

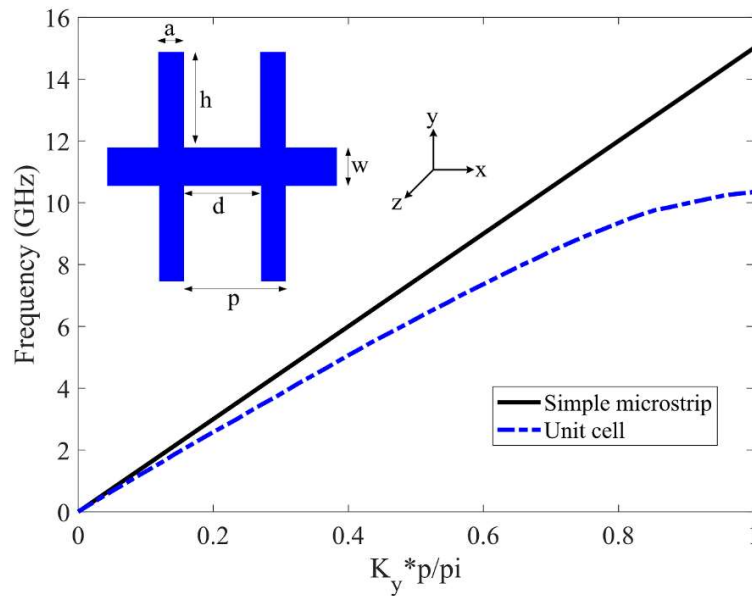


**Figure 6:** Dispersion curves of SSPP unit cell with bilateral grooves.

Propagation properties of guided modes were controlled by its structural parameters: distance between two grooves ( $d$ ), groove height ( $h$ ), metal thickness ( $t$ ) and lattice constant ( $p$ ). Since  $k_y$  deviated from  $k_0$ , there was a mismatch between their momentum and polarization, which led to low productivity. So, a conversion area had to be designed, to achieve gradual conversion, as shown in Fig. 7.

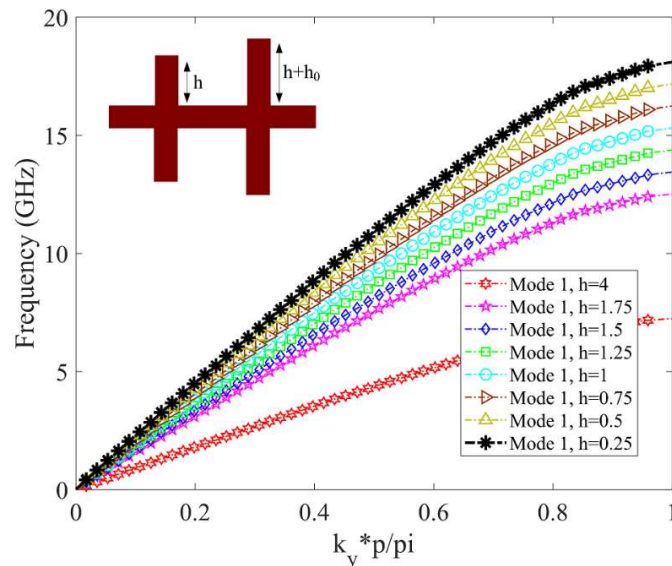


**Figure 7:** Dispersion curves associated with gradual conversion in a SSPP unit cell.

As shown in Fig. 7, grooves height varied from  $h_1$  to  $h_8$ , with equal steps that led to relative adaptations between wave vectors.

On the other hand, the designed filter had a dual-mode frequency response for each parametric analysis with respect to  $l_l$  and  $l_k$  in electromagnetic simulations. To attain relevant results,  $l_l$  was changed by means of  $l_k$ , while remaining physical parameters were kept constant. Odd and even modes changed, so the center frequency moved downward.

According to Fig. 8, odd and even modes changed. So,  $l_k$  was changed by  $l_l$ , while other physical parameters were constant.

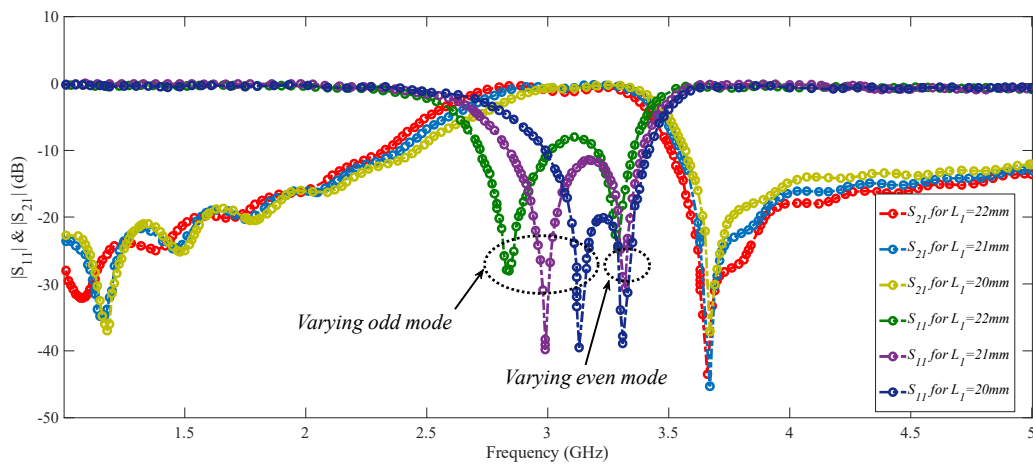


**Figure 8.** Simulation of T-shaped resonator based on BPF with respect to  $l_l$  variation.

As shown in Fig. 9, odd mode was fixed at a specific frequency, but even mode moved to lower frequencies. Hitherto, conditions of the modes were examined. Then, the reflection and passage coefficients were assessed for the designed BPF with different distances (g).

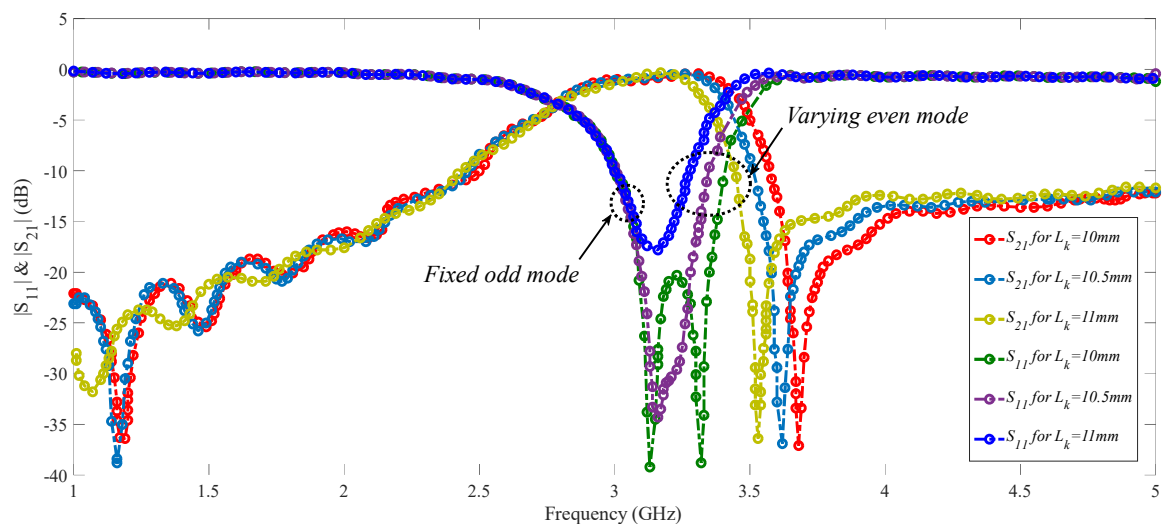


**Figure 9:** Simulation T-shaped resonator based on BPF with respect to  $l_k$  variation.

As shown in Fig. 10, the property of each parameter S was obtained with four different distances. It can be seen that, as the coupled distance increased, input-output connection decreased, due to the small capacity of the distance caused by poor matching.

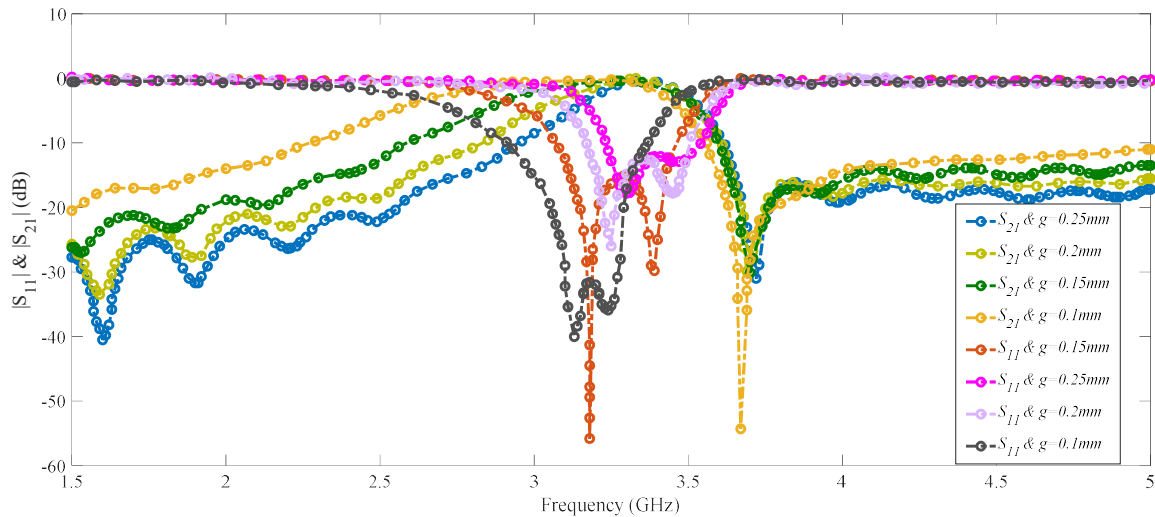


**Figure 10:** S Simulation of T-shaped resonator based on BPF with respect to different distances (g).

The proposed scheme was compared with previous works (Table 1), to verify its performance.

**Table 1:** Comparison of different situations for plasmonic filters.

Ref	Cost-price	Tuning method	Tuning parameter	Method	Description
[15]	High	Static tune	Bandwidth	Bandwidth of the band stop was tuned based on graphene tunable sensor.	A graphene-based suspended nano-strip line was implemented for integrated circuits at terahertz frequencies.
[35]	High	Static tune	Central frequency	Central frequency was tuned by changing dimensions of unit cell.	Thin band-stop and multiple band-stop filters were obtained using CPW based on metal plasmonic waveguides which supported SSPP.
[16]	High	Static tune	Cut-off frequency	Change of capacity value to attain scattering, cut-off frequency and operating band characteristics.	Capacitor of SSPP was to attain scattering reset capability and filtering properties.
[17]	High	Dynamic tune	Central frequency	Variable capacitive components were taken into SSPP unit cell.	Bandwidth characteristics of the SSPP unit cell were tuned.
This paper	Low	Dynamic tune	Central frequency and bandwidth.	Reactors in T-shaped resonator structure to control single and even frequency modes.	Central frequency and BPF tunable bandwidth using T-shaped resonator based on SSPP.

Alternating grooves with metal substrate supported SSPP waves. Using impedance matching theory, a strip SSPP structure was designed by converting the performance of traditional micro-strip lines. Also, a SSPP structure using corrugated grooves was created. Simple meta-material between SSPP and its wave field was returned, due to high electric field intensity under the toothed parts of SSPP strip section. This type of SSPP structure is feasible to design and construct. As for the analysis in this paper, high efficiency of SSPP waves was revealed, which can be a valuable guide to develop these circuits.

Therefore, some strengths, e.g., high accuracy, durability and sensitivity, were confirmed. Additionally, its main drawback is high possibility of sensor surface vulnerability due to oxidation and corrosion.

### **Conclusion**

In this study, spoof plasmonics based BPF using T-shaped resonator was proposed and structured by means of simultaneous reset of the central frequency and bandwidth. The proposed filter proved to be superior to other plasmonic filters with which it was compared. It can accurately work by tuning the dynamics along with the central frequency and bandwidth of the meta-material filter. Simulation results revealed that central frequency moved downwards, and that settlement between s parameters in different modes was achieved. Therefore, the suggested frequency spectrum tunable SSPP filter possesses significant performance and flexibility being practicable to be applied in advanced intelligent systems.

Future research works can include development of thin spoof metalens, providing reliable quality based on the theory of chain dispersion, and emphasis on wide-angle microwave.

### **Funding declaration**

This study did not receive any funding.

### **Data availability**

The analysed data during this study is available upon reasonable request from the corresponding author.

### **Competing interest**

All authors have no financial disclosures and no conflict of interest.

### **Authors' contributions**

All authors have equally contributed for study conception and design.

## **Abbreviations**

**BPF:** band-pass filter

**CST MWS:** CST MICROWAVE STUDIO®

**DC:** direct current

**LRSPP:** long-range surface plasmon polariton

**QTEM:** quasi-transverse electromagnetic

**RF:** radio frequency

**SPP:** surface plasmon polariton

**SRSP:** short-range surface plasmon polariton

**SSPP:** spoof surface plasmon polaritons

**SSP-TL:** spoof surface plasmon transmission line

## **References**

1. Ram GC, Sambaiah P, Yuvaraj S. Graphene based filter design using triangular patch resonator for THz applications. *Nano Communic Netwo.* 2023;38:100477. <https://doi.org/10.1016/j.nancom.2023.100477>
2. Jain S, Choudhary K, Kumar S. Photonic crystal fiber-based SPR sensor for broad range of refractive index sensing applications. *Opt Fib Technol.* 2022;73:103030. <https://doi.org/10.1016/j.yofte.2022.103030>
3. Hajshahvaladi L, Kaatuzian H, Danaie M. A very high-resolution refractive index sensor based on hybrid topology of photonic crystal cavity and plasmonic nested split-ring resonator. *Photon Nanostruc - Fundam Applic.* 2022;51:101042. <https://doi.org/10.1016/j.photonics.2022.101042>
4. Rodrigues EP, Melo AA, Lima AMN. Predicting the Performance of Surface Plasmon Resonance Sensors Based on Anisotropic Substrates. *Plasmonics.* 2021;16:403-412. <https://doi.org/10.1007/s11468-020-01257-w>
5. Suhailin FH, Alwahib AA, Kamil YM. Fiber-based Surface Plasmon Resonance Sensor for Lead Ion Detection in Aqueous Solution. *Plasmonics.* 2020;15:1369-1376. <https://doi.org/10.1007/s11468-020-01160-4>
6. Unutmaz MA, Unlu M. Fixed physical length spoof surface plasmon polariton delay lines for a 2-bit phase shifter. *J Opt Soc Amer B.* 2020;37:1116-1121. <https://doi.org/10.1364/josab.387476>.
7. Yin LZ, Huang TJ, Han FY et al. High-efficiency terahertz spin-decoupled meta-coupler for spoof surface plasmon excitation and beam steering. *Opt Expr.* 2019;27:18928-18939. <https://doi.org/10.1364/OE.27.018928>
8. Hill DA, Johnk RT. Crosstalk between microstrip transmission lines. *IEEE Transact Electromagn Compat.* 1994;36:314-321. <https://doi.org/10.1109/15.328861>
9. Camli B, Yalcinkaya AD. Resonant Type RF Glucose Biosensors. *Encycl Sens Biosens.* 2023;3:308-331. <https://doi.org/10.1016/B978-0-12-822548-6.00011-X>

10. Tian H, Huang G, Xie F et al. THz biosensing applications for clinical laboratories: Bottlenecks and strategies. *Trends Analyt Chem.* 2023;163:117057. <https://doi.org/10.1016/j.trac.2023.117057>
11. Akbar J, Khan A, Abdul M et al. Manipulation of surface plasmon polariton fields excitation at quantum-size slit in a dielectric and graphene interface. *Opt Las Technol.* 2024;170:110234. <https://doi.org/10.1016/j.optlastec.2023.110234>
12. Lingos P, Perrakis G, Tsilipakos O et al. Impact of plasmonic modes on the formation of self-organized nano-patterns in thin films. *Opt Las Technol.* 2023;163:109415. <https://doi.org/10.1016/j.optlastec.2023.109415>
13. Agarwal VM, Viti L, Cupolillo A et al. Plasmonics with two-dimensional semiconductors: from basic research to technological applications. *Nanoscale.* 2018;10:8938-8946. <https://doi.org/10.1039/C8NR01395K>
14. Zhang J, Guan Z, Ma K et al. Perovskite nanowires-based graphene plasmonic waveguides with low loss and low gain threshold. *Diam Rel Mat.* 2023;140:110540. <https://doi.org/10.1016/j.diamond.2023.110540>
15. Singh RS, Sarswat PK. From fundamentals to applications: The development of magnetoplasmonics for next-generation technologies. *Mat Tod Electron.* 2023;4:100033. <https://doi.org/10.1016/j.mtelec.2023.100033>
16. Liang Y, Yu H, Wang H et al. Terahertz metadevices for silicon plasmonics. *Chip.* 2022;1:100030. <https://doi.org/10.1016/j.chip.2022.100030>
17. Wei J, Li W, Niu LY et al. Bendable transmission line and amplifier of spoof surface plasmon polaritons at microwave frequencies. *Opt Expr.* 2023;31:755764. <https://doi.org/10.1364/OE.479642>
18. Anwar RS, Ning H, Mao L. Recent advancements in surface plasmon polaritons-plasmonics in subwavelength structures in microwave and terahertz regimes. *Dig Commun Networ.* 2018;4:244-257. <https://doi.org/10.1016/j.dcan.2017.08.004>
19. Luo J, He J, Apriyana A et al. Tunable Surface-Plasmon-Polariton Filter Constructed By Corrugated Metallic Line and High Permittivity Material. *IEEE Access.* 2018;6:10358-10364. <https://doi.org/10.1109/ACCESS.2018.2800158>
20. Siemion A. Terahertz Diffractive Optics—Smart Control over Radiation. *J Infrac Millim TeraheR Wav.* 2019;40:477-499. <https://doi.org/10.1007/s10762-019-00581-5>
21. Zhao S, Zhao J, Tang WX. An ultra-compact rejection filter based on spoof surface plasmon polaritons. *Sci Rep.* 2017;7:10576. <https://doi.org/10.1109/TCPMT.2017.2700950>
22. Jaiswal RK, Pandit N, Pathak NP. Design, Analysis and Characterization of Designer Surface Plasmon Polariton-Based Dual-Band Antenna. *Plasmonics.* 2018;13:1-10. <https://doi.org/10.1007/s11468-017-0622-1>

23. Farmani A, Omidniaee A. Observation of Plasmonics Talbot effect in graphene nanostructures. *Sci Rep.* 2024;14:1973. <https://doi.org/10.1038/s41598-024-52595-2>
24. Gong S, Bi C, Wang L et al. Dynamic terahertz transmission based on coupling reconfiguration of spoof surface plasmon polaritons. *Opt Expr.* 2022;30:41264-41270. <https://doi.org/10.1364/OE.472959>
25. Varshney AK, Pathak NP, Sircar D. Low-profile metasurface-based dual-band graphene patch nanoantenna. *Nano Commun Networ.* 2023;35:100428. <https://doi.org/10.1016/j.nancom.2022.100428>
26. Tang X, Hu S, Kandwal A et al. Capacitor-loaded spoof surface plasmon for flexible dispersion control and high-selectivity filtering. *IEEE Microwa Wirele Comp Lett.* 2017;27:806-808. <https://doi.org/10.1109/LMWC.2017.2734738>
27. Ye L, Feng H, Li W et al. Ultra-compact spoof surface plasmon polariton waveguides and notch filters based on double-sided parallel-strip lines. *J Phys D: Appl Phys.* 2020;53:265502. <https://doi.org/10.1088/1361-6463/ab7c99>
28. Xu B, Li Z, Liu L et al. Bandwidth tunable microstrip band-stop filters based on localized spoof surface plasmons. *J Opt Soc Amer B.* 2016;33:1388-1391. <https://doi.org/10.1364/JOSAB.33.001388>
29. Zhang HC, Gao X, Tang WX et al. Pass-band reconfigurable spoof surface plasmon polaritons. *J Phys: Cond Matt.* 2018;30:134004. <https://doi.org/10.3390/mi14091687>
30. Brown JA, Barth S, Smyth BP et al. Compact Mechanically Tunable Microstrip Bandstop Filter With Constant Absolute Bandwidth Using an Embedded Metamaterial-Based EBG. *IEEE Transact Microwa Theo Techni.* 2020;68:4369-4380. <https://doi.org/10.1109/TMTT.2020.3016310>
31. Palik ED. *Handbook of Optical Constants of Solids.* New York: Academic. 1985;275. <https://doi.org/10.1016/C2009-0-20920-2>
32. Chen Z, Hooper IR, Sambles JR. Coupled surface plasmons on thin silver gratings. *J Opt A: Pure Appl Opt.* 2007;10:015007. <https://doi.org/10.1088/1464-4258/10/01/015007>
33. Sargent E. Colloidal quantum dot solar cells. *Nat Phot.* 2012;6:133-135. <https://doi.org/10.1021/acs.chemrev.5b00063>
34. Dussopt L. Intermodulation distortion and power handling in RFMEMS switches, varactors and tunable filters. *IEEE Transact Microwa Theo Techni.* 2003;51:1247-1256. <https://doi.org/10.1109/TMTT.2003.809650>
35. Varshney AK, Sircar D. Design of graphenebased THz antennas. *Proceed ICCASP. Adv Intell Syst Comput.* 2019:29-35. [https://doi.org/10.1007/978-981-13-1513-8\\_4](https://doi.org/10.1007/978-981-13-1513-8_4)